Nanoscale

PAPER

View Article Online
View Journal | View Issue

Cite this: *Nanoscale*, 2024, **16**, 1312

Chemically exfoliated boron nanosheets for efficient oxidative dehydrogenation of propane†

Dake Zhang,‡[a] Shenghua Wang,‡[a] Chengcheng Zhang,[b] Le He [b] and Wei Sun *[a]

Received 16th October 2023,
Accepted 5th December 2023

DOI: 10.1039/d3nr05212e

rsc.li/nanoscale

Oxidative dehydrogenation of propane (ODHP) is a promising technique for producing propene due to its low operative temperature and coke-resistant feature. Recently, boron-based catalysts have been widely investigated for ODHP owing to their brilliant performance. Herein, we report that boron in the form of nanosheets can be prepared feasibly by exfoliating layered MgB_2 with hydrochloric acid, and can efficiently and stably catalyze ODHP. At 530 °C, the catalyst exhibits propene and ethene selectivities as high as 63.5% and 18.4%, respectively, at a 40% propane conversion. The olefin productivity reaches 2.48 g_{olefin} g_{cat}^{-1} h^{-1}, superior to the commercial h-BN and other reported boron-based catalysts. Even after testing for 100 h at 530 °C, the catalyst still maintains excellent stability. This work expands the effective boron-based catalyst family for ODHP and demonstrates the great potential of the new type of 2D material-boron nanosheet for energy and catalytic applications.

Introduction

Propene is an imperative raw material used to produce various value-added fine chemicals. Compared with dehydrogenation of propane (PDH), oxidative dehydrogenation of propane (ODHP) is a promising alternative technique for producing propene due to its low operative temperature and coke-resistant feature.[1–4] Recently, boron-based catalysts have shown brilliant performance in ODHP.[5,6] For example, Hermans' group found that hexagonal boron nitride (h-BN) exhibited high propene and ethene selectivities of 79% and 12%, respectively, at a 14% propane conversion.[7] In addition, many reported works have demonstrated that the boron element is indispensable for its high selectivity towards propene in ODHP over boron-based catalysts.[8] In particular, it was confirmed that the BO_x species produced in such boron-based catalysts from surface oxygen functionalization were the main active sites in the reaction process.[9–11] Therefore, it is essential for the further development and design of high-performance catalysts for ODHP to incorporate both the rich content of boron and the feasibility of oxygen functionalization.

Two-dimensional (2D) materials have made great progress in catalytic applications in recent years.[12,13] Belonging to the family of 2D materials, boron nanosheets have attracted tremendous interest due to their remarkable merits (*e.g.*, metallicity, mechanical flexibility, and superconductivity).[14–16] These outstanding physicochemical properties enabled various promising applications such as electronic devices, energy storage, and catalysis.[17–20] The fabrication of boron nanosheets for devices often involved bottom-up growth methods such as chemical vapor deposition (CVD) and mole-

[a]*State Key Laboratory of Silicon Materials and Advanced Semiconductor Materials, and School of Materials Science and Engineering, Zhejiang University, Hangzhou, Zhejiang 310027, People's Republic of China. E-mail: sunnyway423@zju.edu.cn*
[b]*Institute of Functional Nano and Soft Materials (FUNSOM), Jiangsu Key Laboratory for Carbon-Based Functional Materials and Devices, Soochow University, Suzhou 215123, Jiangsu, China*

†Electronic supplementary information (ESI) available. See DOI: https://doi.org/10.1039/d3nr05212e

‡These authors contributed equally to this work.

Wei Sun

Wei Sun currently works at the School of Materials Science and Engineering, Zhejiang University. He completed his PhD and post-doctoral studies in Chemistry-Interdisciplinary under the supervision of Prof. Geoffrey A. Ozin, University of Toronto. His research encompasses silicon-related nanomaterials and nanochemistry for energy, catalytic, and environmental applications, exemplified by photothermal catalysis towards valuable feedstocks. He has been acknowledged as a "Rising Star" by several prominent journals and has won the recognition of the first "Top ten academic progress of youth scholars at Zhejiang University". Owing to his active progress, he has recently been promoted to a tenured Associate Professor.

cular beam epitaxy (MBE).[21,22] However, these delicate methods are not conducive to scaling up. In contrast, the top-down strategy allowing for the synthesis of boron nanosheets with high yield and decent quality is worth investigating for energy and catalysis, which necessitate an adequate amount of ensembles of materials. Recently, a few pioneering works have shown promise in preparing boron nanosheets through top-down methods, including ion exchange,[23] ultrasonication techniques,[24] and liquid-phase exfoliation methods,[25] employing the precursor of layered MgB_2. The as-prepared nanosheets are rich in boron and are easily functionalized by oxygen; thus, they may be high-performance candidates for catalyzing ODHP.

Herein, we report a top-down liquid exfoliation strategy to prepare boron nanosheets by utilizing hydrochloric acid (HCl) as the exfoliating agent and layered MgB_2 as the precursor. After HCl exfoliation, ultrathin and large boron nanosheets can be obtained with a high yield. For the first time, we explored the prepared boron nanosheets as catalysts for ODHP. Owing to the abundant B–O active sites, a brilliant catalytic performance was observed, which is even superior to the commercial h-BN that is well recognized as an efficient catalyst for ODHP. Moreover, the catalytic stability was maintained over 100 h under the high conversion working conditions, a challenge for many other catalysts. Furthermore, the liquid exfoliation strategy can be successfully extended to other boride materials, *e.g.*, AlB_2, which could lead to comparable catalytic performance with the nanosheets exfoliated from MgB_2. Our study demonstrated that exfoliating boride precursors offers an effective approach for synthesizing high-performance catalysts for ODHP, and it is expected to inspire new energy and catalytic applications of 2D boron materials.

Results and discussion

Fig. 1a depicts the fabrication process of boron nanosheets, which consist of boron as the major element but also a small amount of remnant Mg, thus denoted as Mg-BNSs. Briefly, similar to the exfoliation of MXene or silicon nanosheets,[26,27] the Mg-BNSs were produced by selectively etching off the Mg in the layered MgB_2 precursor with HCl. The transmission electron microscopy (TEM) image in Fig. 1b shows the bulk morphology of MgB_2. After HCl etching, the multilayered boron nanosheet stacks can be observed, similar to the morphology of silicon nanosheets obtained from chemical exfoliation,[27,28] indicating leaching of the Mg layers from MgB_2 (Fig. 1c). According to the selected area electron diffraction (SAED), the nanosheets appear to be without high crystallinity (Fig. 1d). Obvious curling can be observed, which indicates the flexible nature of the nanosheets (Fig. 1e). Meanwhile, the thickness of the nanosheets is roughly estimated to be about 5 nm from the TEM image (Fig. 1e). The elemental mappings with energy dispersive X-ray spectroscopy (EDS) of a thin nanosheet show that the Mg, B, and O species were uniformly distributed (Fig. 1f–i), although the signal of

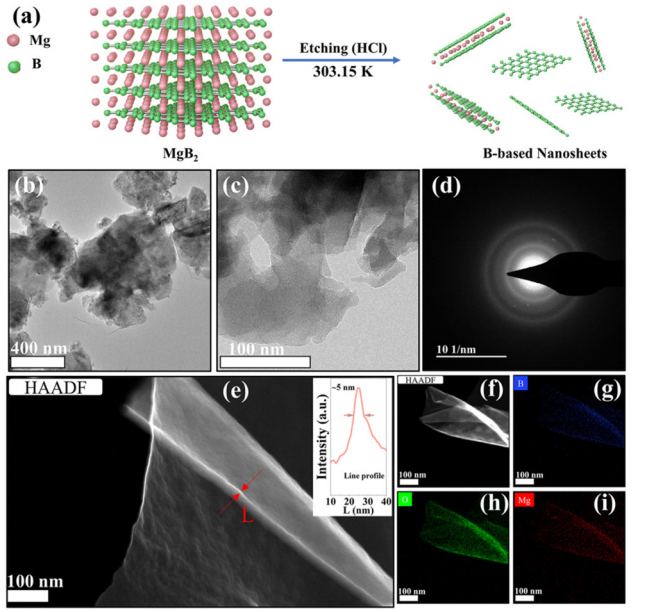

Fig. 1 (a) Schematic illustration for the preparation of boron-based nanosheets. (b) TEM image of MgB_2. (c) TEM image of Mg-BNSs. (d) SAED pattern of Mg-BNSs. (e) HAADF of a thin nanosheet. The inset image is the line profile at position "L". (f–i) EDS mappings of a thin nanosheet.

Mg was weak. Similar distributions were also observed for the ensemble in the elemental mappings associated with scanning electron microscopy (SEM) (Fig. S1†), and the quantitative results showed only 2.21 at% Mg in Mg-BNSs (Fig. S2†). More accurate elemental analysis was conducted with inductively coupled plasma optical emission spectroscopy (ICP-OES). As shown in Table S1,† distinct from pristine MgB_2, the Mg-BNSs exhibited a stoichiometry of $Mg_{0.12}B_2$, indicating that HCl can effectively remove Mg atoms from MgB_2.

X-ray photoelectron spectroscopy (XPS) was employed to further investigate the surface composition and the chemical states of the surface elements before and after the liquid-phase exfoliation. As shown in the survey spectra in Fig. 2a, compared with MgB_2, the B 1s intensity of Mg-BNSs is obviously increased, while the Mg 1s signal becomes obscure, suggesting that most of the Mg atoms have been removed from MgB_2. The Mg 1s peak of Mg-BNSs shifted to a higher energy (from 1303.0 eV to 1303.7 eV) as compared to MgB_2, which indicates that the Mg in Mg-BNSs was in a more oxidized form (Fig. 2b). In addition, the O 1s peak also shifted to a higher energy (Fig. 2c), which can be explained by the higher electronegativity of boron than that of magnesium and the fact that most of the oxygen atoms are attached to boron after the removal of Mg.[29] As to B 1s spectra, there are two peaks for both MgB_2 and Mg-BNSs (Fig. 2d). The main peak at 187.1 eV corresponds to the B–B or B–H bonds, while the peak at 192.0 eV corresponds to the B–O bonds.[8,30,31] The B–O bonds in MgB_2 are formed due to the surface oxidation, as reported previously,[32] and the B–O bonds in Mg-BNSs indicated the pres-

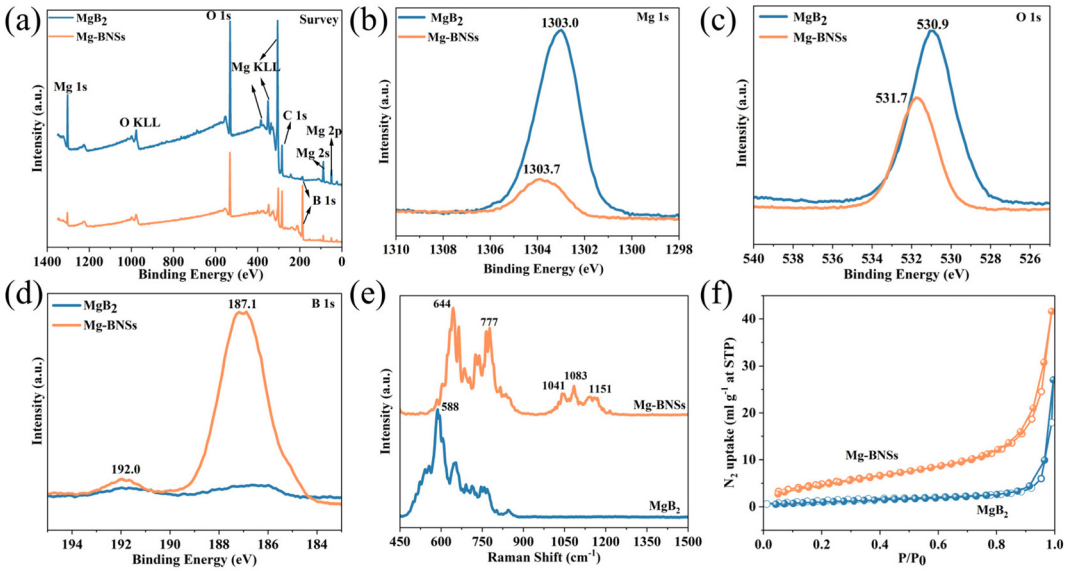

Fig. 2 XPS spectra of (a) survey, (b) Mg 1s, (c) O 1s, and (d) B 1s of MgB_2 and Mg-BNSs. (e) Raman spectra of MgB_2 and Mg-BNSs. (f) N_2 adsorption–desorption curves of MgB_2 and Mg-BNSs.

ence of oxy-functional groups.[33] It is noteworthy that the intensity of B–B or B–H bonds is much higher in the Mg-BNSs as compared with the MgB_2, suggesting that more B atoms were exposed at the surface after acid exfoliation. The elemental composition analysis using XPS further suggests that a significant fraction of interlayer Mg atoms were removed as compared to MgB_2 (Table S2†).

Raman spectroscopy was employed to further differentiate Mg-BNSs from MgB_2 (Fig. 2e). MgB_2 shows a main peak at 588 cm^{-1} ascribed to boron-atom-related E_{2g} phonon mode, as reported previously.[34] In contrast, this mode appeared at a slightly higher wavenumber region for Mg-BNSs (644–777 cm^{-1}). This shift can be ascribed to the disorder of phonon density of states.[35,36] After acid exfoliation, the obtained Mg-BNSs were functionalized by various groups, distinct from the definite MgB_2 structure. In addition, the peaks at 1041, 1083, and 1151 cm^{-1} were ascribed to the different vibration modes of B–H bonds.[30] In short, the Raman spectrum of Mg-BNSs is different from that of MgB_2, suggesting that the obtained Mg-BNS structure has been rearranged owing to the deintercalation of Mg atoms. Meanwhile, as shown in Fig. 2f, the N_2 sorption analyses were employed to explore the surface area of MgB_2 and Mg-BNSs. Mg-BNSs exhibited a higher BET (Brunauer–Emmett–Teller) surface area (18.47 $m^2\ g^{-1}$) than MgB_2 (5.16 $m^2\ g^{-1}$).

As shown above, the obtained Mg-BNSs possessed a significant amount of boron atoms and plenty of B–O sites at the surface, rendering them ideal boron-based catalysts for ODHP. The catalytic tests of ODHP were thus conducted to evaluate the performance of Mg-BNSs in a fixed-bed reactor working at atmospheric pressure. The feeding gas ratio of C_3H_8 and O_2 was maintained at 1 : 1, and N_2 was added as the balance gas. In order to exclude the spontaneous reaction between propane and oxygen at high temperatures, a blank test was also performed, which showed a negligible propane conversion of 1.7% at 540 °C (Fig. S3†).

Next, we explored the performance of MgB_2 and Mg-BNSs for ODHP. As shown in Fig. 3a and Fig. S4,† the propane conversions increase with the temperature. The pristine MgB_2 showed only 4.8% and 6.9% propane conversions at 530 °C and 540 °C, respectively, which were considerably lower than those of Mg-BNSs. As shown in Fig. S5a,† the propene and ethene selectivities were 63.5% and 18.4%, respectively, at a 39.8% propane conversion at 530 °C with Mg-BNSs. It is noteworthy that the total olefin selectivity was greater than 80% with only 0.32% CO_2 produced, which cannot be achieved by metal or metal oxide catalysts at a similar propane conversion. When the temperature rose to 540 °C, a 53.8% propane conversion was obtained with Mg-BNSs. The total olefin selectivity was merely sacrificed, reaching a value of 74.4% (Fig. S5b†). Thus, the total olefin yield was 40.0% (Fig. 3b), highly promising for industrial processes. For further comparison, under the same test conditions, the commercial h-BN, which has been reported in many works and regarded as an excellent and benchmark catalyst for ODHP,[7,37,38] exhibited much lower propane conversions than Mg-BNSs at all temperatures. According to the Arrhenius plots (Fig. 3c), h-BN showed an apparent activation energy (E_a) of 209 kJ mol^{-1}, which was similar to the reported works.[6,39] Meanwhile, Mg-BNSs showed a lower E_a of 185 kJ mol^{-1}, further demonstrating the catalytic excellence of Mg-BNSs. Moreover, as shown in Fig. 3d, compared with typical catalysts, Mg-BNSs exhibited much better olefin productivity. These results manifest that the boron nanosheets prepared with the acid liquid-phase exfoliation method are efficient catalysts for ODHP.

Stability under high-conversion and harsh reaction conditions is an important metric to evaluate catalysts for ODHP.

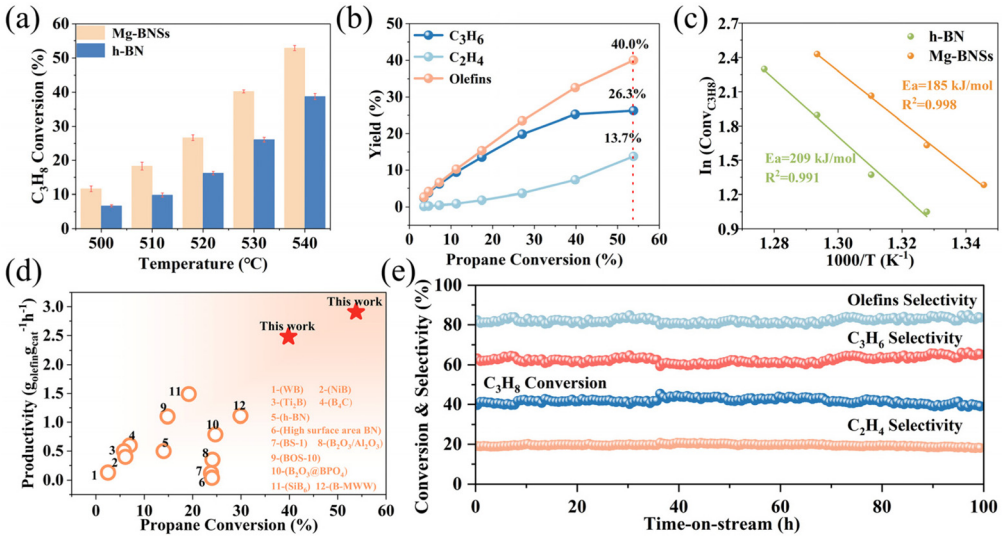

Fig. 3 (a) Catalytic performance of Mg-BNSs and commercial h-BN at different temperatures. (b) Olefin yield as a function of propane conversion over Mg-BNSs. (c) Arrhenius plots of Mg-BNSs and commercial h-BN. (d) Comparison of Mg-BNSs with the reported boron-based catalysts. See Table S3† for specific values. (e) Stability test of Mg-BNSs at 530 °C. Reaction conditions: atmospheric pressure, $C_3H_8/O_2/N_2$ ratio = 1 : 1 : 3, and WHSV = 24 000 ml g^{-1} h^{-1}.

Therefore, a long-time stability test of Mg-BNSs was conducted at 530 °C over 100 h. As shown in Fig. 3e, the catalyst exhibited excellent stability at around 40% propane conversion with an olefin selectivity above 80%, which bodes well for industrial application. Moreover, the carbon balance was 100 ± 3% during the long-term durability test (Fig. S6†). The morphology of Mg-BNSs was maintained after the catalytic test for 100 h, as confirmed by the TEM image and N_2 sorption (Fig. S7 and S8†). By contrast, h-BN showed inferior stability under the same reaction conditions (Fig. S9†). After just a short time of 13 h, the propane conversion decreased notably from 26.8% to 16.3%, although the olefin selectivity slightly increased from 88.5% to 92.1%. XRD patterns identified the emergence of boric acid in the spent h-BN compared with fresh h-BN (Fig. S10†), suggesting the decomposition of h-BN and the tendency of dissolution of B from the B–N bonds, corresponding with the decrease in the propane conversion. A similar phenomenon was observed in other reported literature studies.[6,40]

To further elucidate the origin of the excellent performance of Mg-BNSs, we investigated the dynamic evolution of their structure and surface functional groups under reaction conditions. The rationale of the investigation is supported by the obvious induction period of the activity observed within the first 3 h at 530 °C (Fig. S11†). Thermogravimetric analysis with mass spectroscopy (TG-MS), XRD, and Fourier transform infrared (FT-IR) spectroscopy were employed for Mg-BNSs that endured the reaction atmosphere at different temperatures and durations. As shown in Fig. 4a, noticeable weight loss was observed for fresh Mg-BNSs below 200 °C in the simulated air, ascribed to the dehydration of boron nanosheets. However, mass gain instead began at 400 °C, suggesting that Mg-BNSs can continue to be oxidized under an oxygen-rich atmosphere. By contrast, if the sample was already activated at 500 or 530 °C for over 3 h under the reaction atmosphere, no weight loss could be observed. The results indicate that the oxidized form of nanosheets is responsible for the high performance, which also remains stable under the oxidative atmosphere and does not suffer from coke formation.

As to the XRD analyses, the commercial MgB_2 was confirmed to be highly crystalline, consisting of MgB_2 crystallites and Mg impurity (Fig. S12†). After acid exfoliation, the original structure was destroyed. Upon air exposure, some boron suboxide (B_6O, PDF#87-1143) and B_2O_3 (PDF#76-0781) crystalline phases were observed in Mg-BNSs (Fig. 4b). However, after prolonged reaction, their signals gradually faded and were negligible after 10 h at 530 °C, and thus are not correlated with the stable catalytic performance. In the meantime, crystalline MgO (PDF#45-0946) signals were observed, indicating that the residual Mg atoms were oxidized under the reaction conditions, but MgO is inactive for ODHP. In addition, two new diffraction peaks at 2θ = 17.5° and 19.1° were observed, which matched with the bulk boron (Fig. S13†), indicating that some boron atoms in Mg-BNSs were rearranged to form crystalline boron upon heating.

FT-IR spectra were obtained to probe the oxy-functional groups such as B–O and B–OH that have been reported as active sites for ODHP over boron-based catalysts.[9,41,42] Compared with MgB_2 (Fig. S14†), some new stretching vibrations were observed in Mg-BNSs (Fig. 4c). The B–H stretching modes are near 1620 cm^{-1} and 2500 cm^{-1}, but the intensity of 2500 cm^{-1} is very weak. The three peaks near 1367, 1075 and 860 cm^{-1} are associated with B–O stretching.[23,43,44]

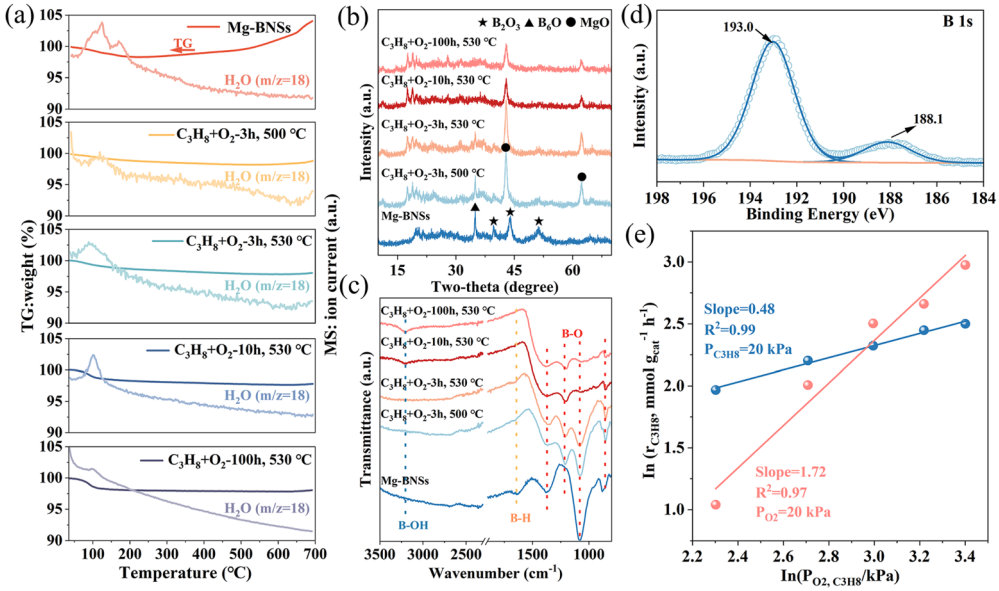

Fig. 4 (a) TG-MS analysis of Mg-BNSs and their spent forms under an O_2-rich atmosphere (20% O_2 + 80% N_2). (b) XRD patterns and (c) FT-IR spectra of Mg-BNSs and the spent Mg-BNSs activated in the reaction atmosphere at different temperatures and durations. (d) B 1s XPS spectrum of Mg-BNSs tested for 100 h over ODHP. (e) Reaction rate as a function of the partial pressure of propane and oxygen in ODHP over Mg-BNSs. The data were obtained at 480 °C.

It is thus concluded that the loss of Mg atoms upon exfoliation was compensated with hydride and oxy-functional groups from the aqueous solution. Similar surface functionalization was observed in other syntheses of nanosheets by utilizing liquid-phase exfoliation, such as MXenes and silicon nanosheets.[45,46] After catalyzing the reaction for 3 h and at 500 °C, the B–H peak almost disappeared and the vibration peak at 1075 cm^{-1} diminished, but a new peak at 1200 cm^{-1} (B–O stretching) emerged. Furthermore, when Mg-BNSs were tested at 530 °C for over 10 h and then cooled down to room temperature, a new peak with B–OH stretching near 3200 cm^{-1} emerged and the peak at 1075 cm^{-1} disappeared, suggesting that the arrangement of B–O bonds has changed significantly during the reaction process. In addition, the decreasing B–O stretching mode at 1075 cm^{-1} was consistent with the diminishment of the B_6O and B_2O_3 phases discussed earlier. Therefore, we speculate that the peak of 1075 cm^{-1} originated from B_6O and B_2O_3. These results indicated that B–OH and B–O bonds (1367, 1200, and 860 cm^{-1}) were the real active sites for ODHP in Mg-BNS catalysts. To supplement, compared to the fresh Mg-BNSs, the spent Mg-BNSs (tested over 100 h at 530 °C) exposed more oxygen atoms at the surface (Table S2†), and exhibited a much more pronounced peak for B–O in the B 1s XPS spectrum (Fig. 4c). These results further confirmed that the catalytic activity was related to the generated B–O sites. Furthermore, kinetic experiments were conducted to study the influence of reactant concentrations on the reaction rate for a better understanding of the active sites. As shown in Fig. 4d, the results show that the reaction orders were 0.48 for oxygen and 1.72 for propane, corresponding with the similar reaction mechanism to h-BN and other reported boron-based catalysts.[5,7,10]

The prepared Mg-BNS catalysts by acid liquid-phase exfoliation of MgB_2 showed excellent performance in ODHP, which motivated us to extend this method to another layered metal boride—AlB_2, and to explore the catalytic performance of the resulting product for ODHP. Interestingly, the pristine AlB_2 showed an initial high propane conversion (37.3%). However, after 10 h, the activity started to decrease. Over a run time of 70 h, the propane conversion decreased to 26.1% (Fig. S15†), which would likely further drop. As shown in Fig. S16,† the reason for the catalytic activity decay of AlB_2 was similar to that of h-BN, as discussed previously. Alternatively, if acid etching was performed, boron nanosheets were obtained (Fig. S17†), denoted as Al-BNSs. The XRD pattern, surface functional groups, and surface area of Al-BNSs were similar to those of Mg-BNSs (Fig. S18†), further suggesting that acid exfoliation of layered metal boride was an effective and general strategy to obtain boron nanosheets. Most importantly, the Al-BNS catalysts exhibited outstanding stability at 530 °C over 100 h with around 41% propane conversion and olefin selectivity at 80 ± 1% (Fig. S19a†). Meanwhile, the carbon balance was maintained at 100 ± 3% during the long-term stability test (Fig. S19b†). These results confirmed that the boron nanosheets as catalysts have huge potential for ODHP under harsh reaction conditions with high conversions. It is noteworthy that the price of MgB_2 is lower than that of AlB_2 (Table S4†). Therefore, MgB_2 as a raw material may be a better choice to produce the

boron-based catalyst for oxidative dehydrogenation of propane.

Experimental section

Materials

All the purchased materials were used without further purification. Magnesium diboride (MgB_2, 99%) and aluminum boride (AlB_2, 99%) were purchased from RHAWN and Acmec, respectively. Hydrochloric acid (36%–38%, analytical reagent) was purchased from Sinopharm Chemical Reagent Co., Ltd. Boron nitride (h-BN) was provided by Tensus Biotech. Milli-Q water (Millipore, 18.2 MΩ cm at 25 °C) was used in all experiments.

Fabrication of boron nanosheets

Mg-BNSs were fabricated by acid-liquid-phase exfoliation. Typically, 1 g of MgB_2 was dispersed into 100 ml of hydrochloric acid in a flask. The mixture was stirred under a N_2 atmosphere at 30 °C for 24 h. Subsequently, the mixture was centrifuged and washed with water and ethanol several times. Finally, the sediments were dried under vacuum and obtained as the product. Similar procedures were followed to prepare Al-BNSs, with AlB_2 as the precursor.

Characterization

The X-ray diffraction (XRD) patterns were obtained using an XRD-700 diffractometer (Shimadzu). Transmission electron microscopy (TEM) images were obtained using an FEI-Tecnai F20 microscope (200 kV). Scanning electron microscopy (SEM) images were obtained using a HITACHI S4800 microscope. The Fourier-transform infrared (FT-IR) spectroscopy spectra were recorded using a Bruker Alpha FTIR spectrometer fitted with a universal attenuated total reflectance sampling accessory. Raman spectra were collected using a HORIBA Scientific LabRAM HR Evolution spectroscope with an excitation wavelength of 532 nm. X-ray photoelectron spectroscopy (XPS) characterization was performed using a Thermo Scientific K-Alpha system equipped with an Al Kα X-ray source ($h\nu$ = 1486.6 eV) and binding energies referenced to C 1s (284.8 eV). The actual contents of Mg and B in the catalysts were measured using an inductively coupled plasma optical emission spectroscope (ICP-OES, Thermo Fisher). Thermogravimetric and mass-spectrometric (TG-MS) results were examined using an STA449-QMS403 spectrometer from NETZSCH. Nitrogen sorption isotherms were recorded at −196 °C on a TriStar II 3020 instrument from micromeritics. The samples were outgassed at 200 °C for 3 h before measurement.

Catalytic performance evaluation

The catalytic performances for oxidative dehydrogenation of propane were evaluated in a fixed-bed reactor under atmospheric pressure. The catalysts (50 mg) were placed in the middle of the quartz tube (I.D. = 6 mm, length = 50 cm) and fixed by quartz wools. A K-type thermocouple was in direct contact with the catalyst and controlled the reaction temperature. The feed gases including C_3H_8, O_2 and N_2 ($C_3H_8 : O_2 : N_2 = 1 : 1 : 3$, total flow rate: 20 ml min^{-1}) were controlled by three mass flow controllers. Reactants and products were analyzed using an online gas chromatograph (FULI INSTRUMENTS, GC9790Plus) equipped with two Porapak Q columns (2 m × 3.175 mm), a 5 Å molecular sieve column (2 m × 4 mm) and an HP-PLOT column (30 m × 0.53 μm × 40 μm). A flame ionization detector (FID) was used to detect C_3H_8, C_3H_6, C_2H_4, C_2H_6, CH_4, *etc*. A thermal conductivity detector (TCD) was used to detect N_2, O_2, CO, and CO_2. The N_2 in the flow was used as the inner standard. The conversion of propane, selectivity of products, yield, and carbon balance were calculated as follows:

$$C_3H_8\ \text{Conversion}(\%) = \frac{\text{C mol of}\left(C_3H_{8,\text{in}} - C_3H_{8,\text{out}}\right)}{\text{C mol of } C_3H_{8,\text{in}}} \times 100\%$$

$$\text{Product selectivity}(\%) = \frac{\text{C mol of a certain product}}{\text{C mol of products}} \times 100\%$$

$$\text{Product yield}(\%) = (\text{propane conversion} \times \text{product selectivity}) \times 100\%$$

$$\text{Carbon balance}(\%) = \frac{\text{C mol of}(\text{products} + C_3H_{8,\text{out}})}{\text{C mol of } C_3H_{8,\text{in}}} \times 100\%$$

where C mol represents the mole number of carbons in feed gases and effluent gases.

Conclusions

In summary, we have successfully constructed ultrathin and large boron nanosheets by acid liquid-phase exfoliation of MgB_2. The boron nanosheets were easily functionalized with hydride and oxy-functional groups. Their application as an effective catalyst for ODHP was explored for the first time. The catalyst showed a 40% propane conversion at 530 °C with propene and ethene selectivities as high as 63.5% and 18.4%, respectively. Moreover, it exhibited a 32.5% olefin yield at a stable 39.8% propane conversion over 100 h, which is higher than those of h-BN and other reported boron-based catalysts, and highly promising for actual industrial implementation. TG-MS, FT-IR, and XRD techniques confirmed that the boron nanosheets transformed into a thermally stable structure during the reaction process and the B–O/B–OH sites were the active centers for ODHP. Moreover, the preparation and high catalytic performance for ODHP can also be extended to using other layer metal borides as the precursor, such as AlB_2. Our study demonstrated that the boron nanosheets exfoliated from a boride precursor possess the demanded structure and functionalities that conform to the advanced catalyst design for high performance in ODHP. It may inspire further advances in applications of new types of 2D boron materials.

Author contributions

D.Z. and S.W. contributed to this work equally as co-first authors. W.S., D.Z., and S.W. carried out the synthesis and catalysis experiments, analyzed the data, and prepared the manuscript. C.Z. and L.H. carried out the TEM characterization and analysis. All authors commented on the final manuscript.

Conflicts of interest

There are no conflicts to declare.

Acknowledgements

The authors acknowledge the support from the National Natural Science Foundation of China (52372233, 61721005), the Fundamental Research Funds for the Central Universities (226-2022-00159, 226-2022-00200), and the U of T-ZJU Joint Seed Fund.

References

1 J. Sheng, B. Yan, W. D. Lu, B. Qiu, X. Q. Gao, D. Wang and A. H. Lu, *Chem. Soc. Rev.*, 2021, **50**, 1438–1468.
2 L. Shi, D. Wang and A.-H. Lu, *Chin. J. Catal.*, 2018, **39**, 908–913.
3 J. M. Venegas, W. P. McDermott and I. Hermans, *Acc. Chem. Res.*, 2018, **51**, 2556–2564.
4 Z.-Y. Wang, Z.-H. He, L.-Y. Li, S.-Y. Yang, M.-X. He, Y.-C. Sun, K. Wang, J.-G. Chen and Z.-T. Liu, *Rare Met.*, 2022, **41**, 2129–2152.
5 W.-D. Lu, D. Wang, Z. Zhao, W. Song, W.-C. Li and A.-H. Lu, *ACS Catal.*, 2019, **9**, 8263–8270.
6 H. Zhou, X. F. Yi, Y. Hui, L. Wang, W. Chen, Y. C. Qin, M. Wang, J. B. Ma, X. F. Chu, Y. Q. Wang, X. Hong, Z. F. Chen, X. J. Meng, H. Wang, Q. Y. Zhu, L. J. Song, A. M. Zheng and F. S. Xiao, *Science*, 2021, **372**, 76–80.
7 J. T. Grant, C. A. Carrero, F. Goeltl, J. Venegas, P. Mueller, S. P. Burt, S. E. Specht, W. P. McDermott, A. Chieregato and I. Hermans, *Science*, 2016, **354**, 1570–1573.
8 J. T. Grant, W. P. McDermott, J. M. Venegas, S. P. Burt, J. Micka, S. P. Phivilay, C. A. Carrero and I. Hermans, *ChemCatChem*, 2017, **9**, 3623–3626.
9 H. Yan, S. Alayoglu, W. Wu, Y. Zhang, E. Weitz, P. C. Stair and J. M. Notestein, *ACS Catal.*, 2021, **11**, 9370–9376.
10 L. Cao, P. Dai, J. Tang, D. Li, R. Chen, D. Liu, X. Gu, L. Li, Y. Bando, Y. S. Ok, X. Zhao and Y. Yamauchi, *J. Am. Chem. Soc.*, 2020, **142**, 8755–8762.
11 R. W. Dorn, L. O. Mark, I. Hung, M. C. Cendejas, Y. Xu, P. L. Gor'kov, W. Mao, F. Ibrahim, Z. Gan, I. Hermans and A. J. Rossini, *J. Am. Chem. Soc.*, 2022, **144**, 18766–18771.
12 M. Zhao, T. Li, L. Jia, H. Li, W. Yuan and C. M. Li, *ChemSusChem*, 2019, **12**, 5041–5050.
13 X. Fan, M. Zhao, T. Li, L. Y. Zhang, M. Jing, W. Yuan and C. M. Li, *Nanoscale*, 2021, **13**, 18332–18339.
14 F. R. Fan, R. X. Wang, H. Zhang and W. Z. Wu, *Chem. Soc. Rev.*, 2021, **50**, 10983–11031.
15 C. Han, R. Han, X. Zhang, Z. Xu, W. Li, Y. Yamauchi and Z. Huang, *J. Mater. Chem. A*, 2022, **10**, 2736–2750.
16 X. Sun, X. Liu, J. Yin, J. Yu, Y. Li, Y. Hang, X. Zhou, M. Yu, J. Li, G. Tai and W. Guo, *Adv. Funct. Mater.*, 2017, **27**, 1603300.
17 A. J. Mannix, Z. Zhang, N. P. Guisinger, B. I. Yakobson and M. C. Hersam, *Nat. Nanotechnol.*, 2018, **13**, 444–450.
18 S. Y. Xie, Y. Wang and X. B. Li, *Adv. Mater.*, 2019, **31**, 1900392.
19 A. Fujino, S. I. Ito, T. Goto, R. Ishibiki, J. N. Kondo, T. Fujitani, J. Nakamura, H. Hosono and T. Kondo, *ACS Omega*, 2019, **4**, 14100–14104.
20 T. Goto, S.-i. Ito, S. L. Shinde, R. Ishibiki, Y. Hikita, I. Matsuda, I. Hamada, H. Hosono and T. Kondo, *Commun. Chem.*, 2022, **5**, 118.
21 G. Tai, T. Hu, Y. Zhou, X. Wang, J. Kong, T. Zeng, Y. You and Q. Wang, *Angew. Chem., Int. Ed.*, 2015, **54**, 15473–15477.
22 A. J. Mannix, X.-F. Zhou, B. Kiraly, J. D. Wood, D. Alducin, B. D. Myers, X. Liu, B. L. Fisher, U. Santiago, J. R. Guest, M. J. Yacaman, A. Ponce, A. R. Oganov, M. C. Hersam and N. P. Guisinger, *Science*, 2015, **350**, 1513–1516.
23 H. Nishino, T. Fujita, N. T. Cuong, S. Tominaka, M. Miyauchi, S. Iimura, A. Hirata, N. Umezawa, S. Okada, E. Nishibori, A. Fujino, T. Fujimori, S. I. Ito, J. Nakamura, H. Hosono and T. Kondo, *J. Am. Chem. Soc.*, 2017, **139**, 13761–13769.
24 H. Nishino, T. Fujita, A. Yamamoto, T. Fujimori, A. Fujino, S.-i. Ito, J. Nakamura, H. Hosono and T. Kondo, *J. Phys. Chem. C*, 2017, **121**, 10587–10593.
25 S. K. Das and K. Jasuja, *ACS Appl. Nano Mater.*, 2018, **1**, 1612–1622.
26 Z. Wu, J. Shen, C. Li, C. Zhang, K. Feng, Z. Wang, X. Wang, D. M. Meira, M. Cai, D. Zhang, S. Wang, M. Chu, J. Chen, Y. Xi, L. Zhang, T.-K. Sham, A. Genest, G. Rupprechter, X. Zhang and L. He, *ACS Nano*, 2022, **17**, 1550–1559.
27 X. Yan, W. Sun, L. Fan, P. N. Duchesne, W. Wang, C. Kubel, D. Wang, S. G. H. Kumar, Y. F. Li, A. Tavasoli, T. E. Wood, D. L. H. Hung, L. Wan, L. Wang, R. Song, J. Guo, I. Gourevich, A. A. Jelle, J. Lu, R. Li, B. D. Hatton and G. A. Ozin, *Nat. Commun.*, 2019, **10**, 2608.
28 C. Wang, X. Xu, X. Pi, M. D. Butala, W. Huang, L. Yin, W. Peng, M. Ali, S. C. Bodepudi, X. Qiao, Y. Xu, W. Sun and D. Yang, *Nat. Commun.*, 2022, **13**, 5216.
29 A. Talapatra, S. K. Bandyopadhyay, P. Sen, P. Barat, S. Mukherjee and M. Mukherjee, *Phys. C*, 2005, **419**, 141–147.
30 C. Hou, G. Tai, J. Hao, L. Sheng, B. Liu and Z. Wu, *Angew. Chem., Int. Ed.*, 2020, **59**, 10819–10825.
31 R. Kawamura, N. T. Cuong, T. Fujita, R. Ishibiki, T. Hirabayashi, A. Yamaguchi, I. Matsuda, S. Okada, T. Kondo and M. Miyauchi, *Nat. Commun.*, 2019, **10**, 4880.

32 K. B. Garg, T. Chatterji, S. Dalela, M. Heinonnen, J. Leiro, B. Dalela and R. K. Singhal, *Solid State Commun.*, 2004, **131**, 343–347.
33 A. L. James and K. Jasuja, *RSC Adv.*, 2017, **7**, 1905–1914.
34 A. Bateni, E. Erdem, W. Häßler and M. Somer, *AIP Adv.*, 2019, **9**, 045018.
35 W. X. Li, Y. Li, R. H. Chen, R. Zeng, S. X. Dou, M. Y. Zhu and H. M. Jin, *Phys. Rev. B: Condens. Matter Mater. Phys*, 2008, **77**, 094517.
36 A. Bateni, E. Erdem, S. Repp, S. Acar, I. Kokal, W. Häßler, S. Weber and M. Somer, *J. Appl. Phys.*, 2015, **117**, 153905.
37 P. Chaturbedy, M. Ahamed and M. Eswaramoorthy, *ACS Omega*, 2018, **3**, 369–374.
38 Z. Liu, B. Yan, S. Meng, R. Liu, W. D. Lu, J. Sheng, Y. Yi and A. H. Lu, *Angew. Chem., Int. Ed.*, 2021, **60**, 19691–19695.
39 L. Shi, D. Wang, W. Song, D. Shao, W.-P. Zhang and A.-H. Lu, *ChemCatChem*, 2017, **9**, 1788–1793.
40 L. Cao, P. Yan, S. Wen, W. Bao, Y. Jiang, Q. Zhang, N. Yu, Y. Zhang, K. Cao, P. Dai and J. Xie, *J. Am. Chem. Soc.*, 2023, **145**, 6184–6193.
41 X. Cheng, Y. Zhang, J. Wang, X. Zhang, C. Sun, Y. Yang and X. Wang, *ACS Catal.*, 2023, **13**, 1630–1637.
42 P. Li, X. Zhang, J. Wang, Y. Xue, Y. Yao, S. Chai, B. Zhou, X. Wang, N. Zheng and J. Yao, *J. Am. Chem. Soc.*, 2022, **144**, 5930–5936.
43 P. Rohani, S. Kim and M. T. Swihart, *Adv. Energy Mater.*, 2016, **6**, 1502550.
44 A. I. Kharlamov and N. V. Kirillova, *Powder Metall. Met. Ceram.*, 2002, **41**, 97–106.
45 M. Naguib, O. Mashtalir, J. Carle, V. Presser, J. Lu, L. Hultman, Y. Gogotsi and M. W. Barsoum, *ACS Nano*, 2012, **6**, 1322–1331.
46 H. Nakano, T. Mitsuoka, M. Harada, K. Horibuchi, H. Nozaki, N. Takahashi, T. Nonaka, Y. Seno and H. Nakamura, *Angew. Chem., Int. Ed.*, 2006, **45**, 6303–6306.